



ORIGINAL RESEARCH ARTICLE

Microstructural Evolution and Mechanical Properties of AZ31 Magnesium Alloy Processed through Constrained Groove Pressing at Different Deformations and Temperatures

Li Yu

Submitted: 30 June 2023 / Revised: 1 December 2023 / Accepted: 7 December 2023

In this study, severe plastic deformation through the constrained groove pressing (CGP) method followed by an annealing operation was applied to the AZ31 Mg alloy sheets to improve their microstructural and mechanical properties. Accordingly, the sample is repeatedly deformed at high temperatures through a scheduled pressing succession to accelerate grain refinement. Investigating the deformation and temperature successions in the CGP process indicated their significant dependence on the microstructure characterization and mechanical properties. Also, processing temperature reduction restricted static recovery, recrystallization, and grain growth, leading to the development of fine- and ultrafine-grained structures. Hence, the appropriate selection of deformation and temperature successions can thoroughly affect the total strain, texture evolution, and grain refinement. Therefore, such a thermomechanical treatment can be extended to a broad range of materials.

Keywords anisotropy, deformation route, severe plastic deformation, temperature succession, texture

1. Introduction

It has been found that magnesium (Mg) and its alloy forms do not show adequate formability at ambient temperature due to the associated hcp crystalline structure and the low amount of active slip systems (Ref 1-3). On the other hand, as is known, at least five independent slip systems are required to meet the Von Mises criteria to have a homogeneous plastic deformation. At the ambient temperature, the plastic deformation of Mg is restricted to $\{0001\} \langle 11-20 \rangle$ with basal type of $\langle a \rangle$ slip, while non-basal slip forms and twinning participate slightly in plastic deformation. In addition, the base $\langle a \rangle$ slip has solely two independent slip systems that cannot satisfy the Von Mises criteria; consequently, Mg possesses significantly low formability at the ambient temperature (Ref 4, 5). If more plastic deformation is needed for Mg alloys, further non-basal slip systems such as $\{10-10\} \langle 11-20 \rangle$ prismatic $\langle a \rangle$ slip, first-order $\{10-11\} \langle 11-20 \rangle$ pyramidal $\langle a \rangle$ slip, and second-order $\{11-22\} \langle 11-23 \rangle$ pyramidal $\langle c + a \rangle$ slip should be involved. However, the non-basal slip groups need a higher critical resolved shear stress (CRSS) and generally activate at temperatures above 250 °C (Ref 6, 7).

On the other hand, unfavorable texture changes during the plastic deformation of Mg alloys can limit their formability. For

example, there is a strong basal texture in rolled or extruded Mg sheets or bars in the rolling and extrusion directions, respectively. By applying compressive loads to the directions in the hcp structure, a tensile strain is imposed on the c-axis, which causes an activation of the $\{10-12\}$ extension twinning in the entire material. As a result, the c-axis rotates 86.3° from its initial direction and aligns near the compression axis (Ref 6, 8-10). It should be noted that the next plastic deformation can just be adjusted along the c-axis, while due to the absence of a deformation mechanism, it will be along the c-axis. Likewise, compression strains are imposed on the c-axis by applying the tensile form of loads to the extrusion or rolling direction, enabling $\{10-11\}$ contraction. In this way, very little thinning of the sheet occurs without the occurrence of any rotation in the hcp crystals (Ref 11-14). Hereon, the orientation of grains favors prismatic $\langle a \rangle$ slip. Nevertheless, prismatic $\langle a \rangle$ slip at ambient temperature cannot be activated due to the high value of critical resolved shear stress (CRSS) compared to basal slip (Ref 11, 15, 16).

So far, the severe plastic deformation (SPD) technique has been widely recognized as an effective approach in a comprehensive range of bulk single and polycrystalline materials to obtain ultrafine-grained (UFG) and even nanostructured (NS) metals and alloys (Ref 17-20). Therefore, it has become possible to produce grains from about 1 μm to less than 100 nm, depending on the type of materials, the SPD technique, and their processing requirements. Such a significant decrease in grain size can have substantial consequences because, since long ago, grain refinement has often been used to enhance the mechanical performance properties of the materials, like toughness and strength (Ref 21-24). The yield strength in metals and alloys changes with grain size based on the Hall-Petch relationship (Ref 25-28). In this regard, UFG/NS materials can prevent dislocation movement, and consequently,

Li Yu, Jiangsu Vocational Institute of Architectural Technology, Xuzhou, Jiangsu, China. Contact e-mail: jsjzixb@163.com.

increase strength due to having larger grain boundary areas. Among the various SPD techniques, equal channel angular pressing (Ref 29), equal channel forward extrusion (Ref 30), high-pressure torsion (Ref 31), multidirectional forging (Ref 32), accumulative roll bonding (Ref 33), constrained groove pressing (Ref 34), and planar twist extrusion (Ref 35) are well known.

For the first time, Shin and co-workers proposed a constrained groove pressing (CGP) method, schematically shown in Fig. 1 (Ref 36). In the first pass of the CGP technique, a properly lubricated sheet is pressed between the grooved dies (see Fig. 1a and b) to be deformed into the shape of these dies. In this circumstance, although the material in the inclined region undergoes deformation (simple shear type), the material's flat region will remain plastically unchanged (end of the first pass). The second pass consists of a flattening step to return the deformed sheet to its original shape with the help of flat dies; see Fig. 1(c). Next, the sheet should be rotated 180° around its normal axis until the undeformed region of the specimen can be subjected to the same shear processing with the help of the same grooved dies (Fig. 1d and e) until uniform plastic strain occurs throughout the material (end of the third pass). Finally, the fourth pass is performed by the flat dies to restore the original shape of the deformed material (Fig. 1f). Hence, a full cycle consists of a total of four passes to fabricate a homogeneous shear strain throughout the material. Note that in most cases, the above passes are repeated for more cycles to apply a high enough plastic strain to refine the grain size (Ref 37-41).

So far, various studies have been carried out on the CGP processing of different magnesium alloys (Ref 42-47). The result of an alternate biaxial reverse corrugation process, which is a derived method like CGP, was investigated by Yang and Ghosh (Ref 48) on the AZ31B Mg samples. The results showed that a cumulative plastic strain of 5.0 resulted in a uniform mean grain size of about 1.5 μm . Furthermore, the tensile strength and elongation-to-failure of the processed sample reached 280 MPa and 22.6%, respectively. Intensive grain refinement also led to a decrease in the tensile-compressive

yield-strength difference. In this regard, the improvement of tensile-compressive inhomogeneity can be associated with the deduction of twinning occurrence in the UFGed alloy and during the in-plane compression. In a similar experiment on the AZ31 alloy by Huo et al. (Ref 49), with the help of a sin-wave die, a 45° rotation was successfully performed at every pass. After four passes of 400 °C bending, the mean grain size was decreased to about 8 μm , and the ambient temperature fracture elongation was enhanced to about 25%. In addition, texture randomization was detectable after four bending passes. Finally, the increase in the Erichsen value to 2.7 indicated better formability of the produced sample. In a study by Miura et al. (Ref 50), they investigated the multidirectional forging of the AZ31 Mg alloy at different processing temperatures. By reducing the processing temperature from 350 to 150 °C, the mean final grain size reached 0.37 μm at the total plastic strain of 5, which includes the basal texture around 90° to the final compression axis. By performing the tensile test in different orientations of 0, 45, and 90° relative to the final compression axis at a temperature of 150 °C, the yield strength anisotropy in different directions at a low strain rate is less compared to the higher strain rate. The impact of the equal channel angular pressing method on the properties of squeezed-cast AZ31 Mg alloy was investigated by Janeček et al. (Ref 51). The results indicated an increase of more than two times at room temperature in compressive yield strength. However, the compressive yield strength at temperatures above 200 °C became lower than that of the initial one. The alloying effect through lanthanum-rich mischmetal and calcium addition after the application of the ECAP method on the AZ31 magnesium alloy was studied by Masoudpanah and Mahmudi (Ref 52). It was found that the addition of lanthanum-rich mischmetal and calcium causes a slight decrease in both grain size and tensile elongation. In the research of Zamina et al. (Ref 53), twin roll cast AZ31 magnesium was used for the CGP process. It was found that the initial sample has a heterogeneous hardness distribution, while a substantial difference is attainable in the rolling direction of the CGP-processed sample. However, the microhardness remained almost constant in the normal direction. In the study by Wang et al. (Ref 54) on two-pass CGP processing of AZ31 magnesium alloy, a bimodal structure was developed due to partial dynamic recrystallization and deformation homogeneity. In this regard, the maximum elongation to failure of 38.7% was obtained at $1 \times 10^{-4} \text{ s}^{-1}$ and 473 K, while the yield and tensile strengths were 37 and 43 MPa, respectively. Zimina et al. (Ref 53) and Thuy et al. (Ref 55) showed that the CGP technique is a suitable tool for the grain refinement of magnesium alloys. Accordingly, the microstructure of the CGP-processed twin-roll cast AZ31 magnesium strips exhibited a significant reduction of the grain size from 200 to 20 μm . In addition, the microhardness inhomogeneities along the cross-section of the as-cast strip were replaced by bands of different microhardness in the processed material. The simulation of the CGP process by Lin et al. (Ref 56) revealed that the effective strain distribution of the AZ31 sheet was homogeneous after four cycles at 473 K. During the CGP process of the AZ31 magnesium alloy for up to three cycles in the temperature range of 503-448 K, a homogeneous fine-grained microstructure was attained with an average grain size of 1.8 μm (Ref 57). It should be noted that a significant portion of low-angle grain boundaries (subgrains) and dislocation boundaries, which persisted in the structure as a result of

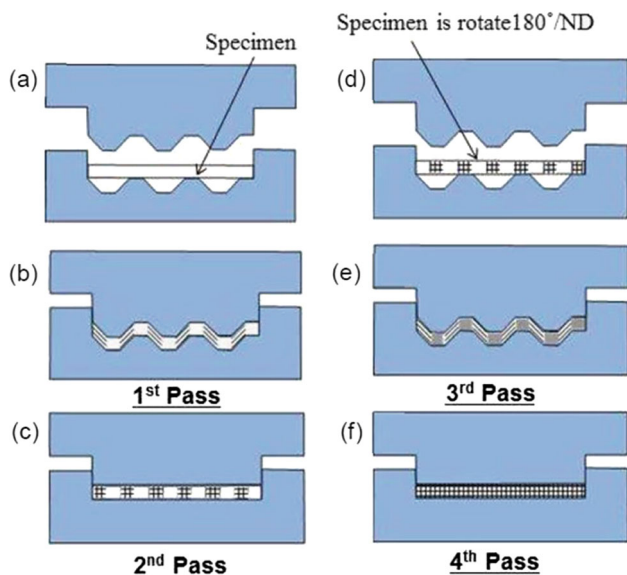


Fig. 1 Schematic diagram for the stages of the constrained groove pressing (CGP) process

insufficient dynamic recovery and recrystallization, were identified in the CGP-processed microstructure.

According to previous studies (Ref 18, 58-61), it can be deduced that the low formability of Mg alloy is an ordinary research challenge. So, it is feasible to enhance formability through grain refinement and the weakening of the strong basal texture. The study of SPD on wrought AZ31 sheets, especially using the CGP method, has been very limited. Therefore, the wrought AZ31 sheet is selected for this research due to its availability. It should be noted that if the problem of low ductility of Mg sheets is solved, their widespread use for forming processes will expand day by day.

2. Materials and Method

For this study, the AZ31 Mg alloy with the chemical composition listed in Table 1 was selected because of its wide applications in the automotive and aerospace industries. Also, all alloying elements constitute a solid solution in a magnesium matrix, so the lack of intermetallic particles makes it easy to investigate the plastic deformation and strengthening mechanisms after the CGP process. In this research, a 2 mm-thick hot-rolled AZ31 sheet was utilized in the annealed state. Its yield (YS), ultimate tensile strength (UTS), and mean elongation were approximately 150 MPa, 251 MPa, and 20% at ambient temperature. For the CGP experimentation, the sheet was sectioned into 12 mm × 12 mm square-shaped samples.

The CGP process was carried out through a hydraulic press with a pressing rate of about 4 mm/s and a pair of grooved and flat dies at high temperatures. The grooved distance and angle were equal to 2 mm and 45°, respectively. In addition, the pressing was conducted at elevated temperatures.

Two CGP deformation successions of “D_A” and “D_B” and two CGP processing temperatures of “T_A” and “T_B” were chosen for this study. The schematic representation of the applied deformation succession is shown in Fig. 2. The sample is rotated 90° in the “D_A” route before beginning each deformation cycle. While in route “D_B”, the sample is deformed in an orthogonal manner enclosed by the grooved dies four times prior to being flattened in the last stage. Therefore, the major distinction between these two routes is that “D_B” is not supposed to experience an intermediate flattening process during the deformation cycle. Furthermore, the deformation temperature in the T_A method gradually decreased after each processing step, so that the minimum temperature of deformation was estimated empirically under the material’s workability in preventing fracture. The deformation temperature was 250 °C in the first cycle, 200 °C in the second cycle, and 150 °C in the final two cycles. In the “T_B” method, the temperature of the deformation was kept constant between 200 and 300 °C during the deformation cycles. According to the mentioned deformation succession and

Table 1 The chemical composition of AZ31B-O by wt.% used in this research

Element	Mg	Al	Zn	Mn	Si	Cu	Fe
Mass, %	Bal.	2.91	0.58	0.25	0.07	0.06	0.03

processing temperature, six samples with different conditions listed in Table 2 were designed for this study in such a way as to permit a useful comparison for investigating the result of thermal and deformational successions on their microstructure and mechanical characteristics.

The microstructure of the samples was evaluated by a GX51 Olympus inverted optical microscope (OM) before and after the process in a parallel plane to the sheet surface and in cross-sectional thickness. For this purpose, the samples were divided into smaller ones. They were then ground up to 4000 grits SiC paper and polished using diamond particle slurry. The polished samples were washed ultrasonically for 5 minutes, and microstructure images were obtained by chemical etching in a picric acid solution. Finally, the average grain size was determined by the linear intercept method based on the ASTM-E112 standard. To measure texture properties using an x-ray diffractometer, specimens were prepared with dimensions of 15 mm × 15 mm from the center of the initial and processed samples with different deformation and temperature successions. The partial pole figures of the basal {0002}, prismatic {10-10}, and pyramidal {10-11} planes were obtained on the various reflection angles of 30-39° (tilt angle of 70°) by x-ray diffractometer at 40 kV and 35 mA through reflection geometry with the Cu-K_α radiation. The intensity values of the diffractions were subsequently normalized, and functions of orientation distribution were determined from the partial pole figures. Tensile specimens were prepared along two planes in the rolling and transverse directions under the ASTM-E8M standard with a gauge length, width, and thickness of 25 mm, 6 mm, and 1.2 mm. Ambient-temperature tensile experiments were conducted utilizing an Instron 3400 machine with an initial strain rate of 1.5 × 10⁻³. In addition, the hardness measurement (Matsuzawa MMTX3) was carried out throughout the specimen thickness with the help of a micro-Vickers hardness tester under a load of 100 g. It should be noted that the mechanical anisotropy of the initial and processed sheets was studied by ambient temperature tensile experiments performed in three directions: transverse, 45°, and rolling. The anisotropy level of the in-plane and thickness was determined using the ratio of plastic strain, *r*-value, determined at 8% engineering strain value for Mg alloys, based on Ref 62.

3. Results and Discussion

3.1 Microstructure Characterization

Figure 3a and b illustrate the initial microstructure of the initial annealed AZ31. The microstructures have been performed along two rolling and transverse directions (RD and TD) at the thickness of the sample. As revealed in Figs. 3(a) and (b), the microstructures are relatively equiaxed and uniform in both directions, and the mean grain size is 14 μm. Also, as shown in Fig. 3(c), (d), (e) and (f), the “S₁” sample was investigated to disclose the microstructure evolution of every CGP cycle.

As shown in Fig. 3(c), the grain size in the first cycle of the process, performed at 250 °C, was remarkably decreased, and the mean grain size reached 6.5 μm, representing a reduction of about 53% in the initial grain size. The first-cycle microstructure is not uniform because of the incomplete dynamic recrystallization. Therefore, numerous newly generated refined

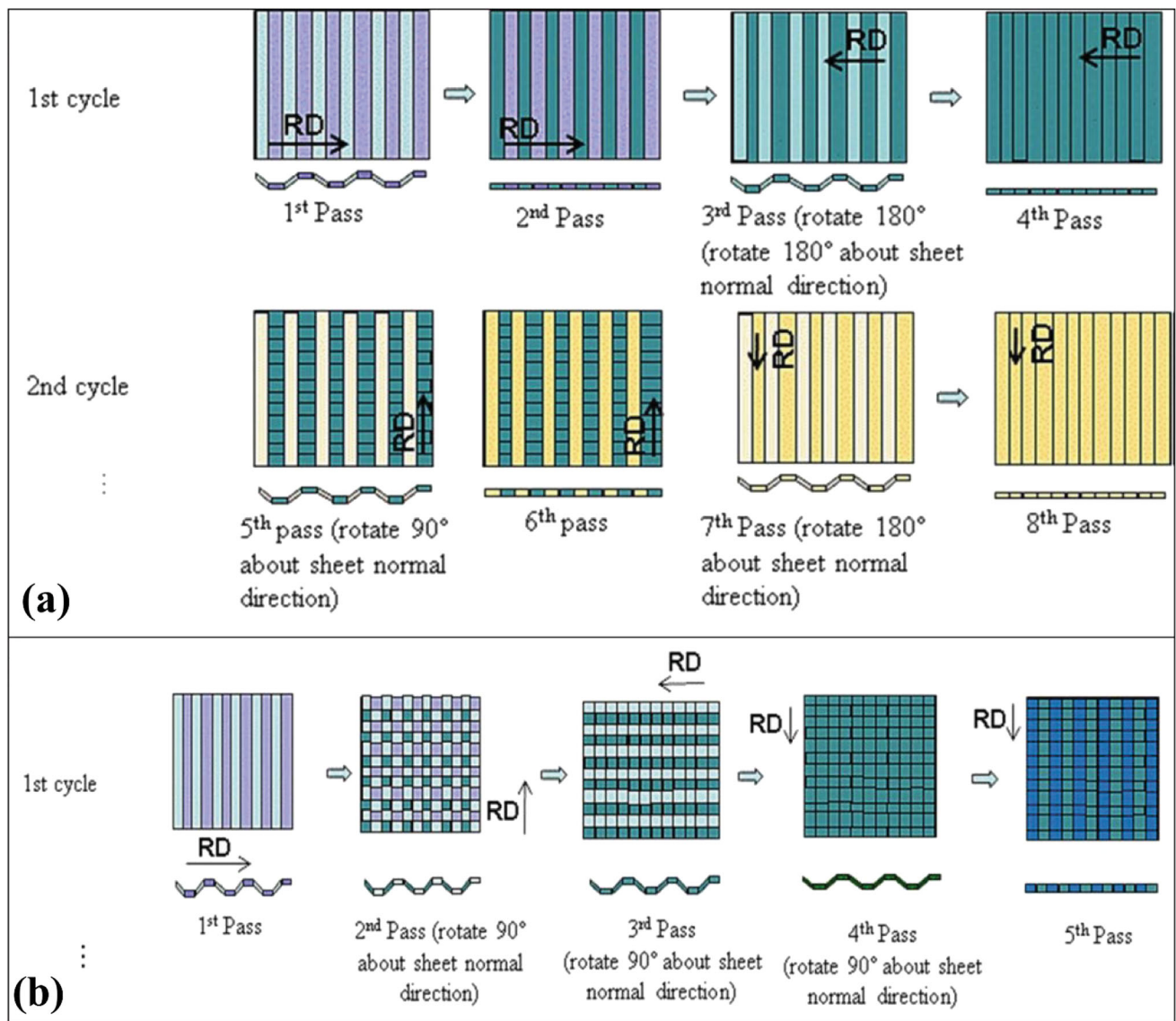


Fig. 2 Schematic representation of the deformation successions, including (a) the first two deformation cycles in the “D_A” method and (b) the first deformation cycle in the “D_B” method

Table 2 Mg alloy preparation conditions subjected to diverse thermal and deformation successions

Sample designation	Deformation successions	Number of cycles	Temperature successions
“S ₁ ”	“D _A ”	4	“T _A ” (1st cycle at 250 °C, 2nd cycle at 200 °C, and last two cycles at 150 °C)
“S ₂ ”	“D _A ”	4	“T _B ” (200 °C)
“S ₃ ”	“D _A ”	4	“T _B ” (250 °C)
“S ₄ ”	“D _A ”	4	“T _B ” (300 °C)
“S ₅ ”	“D _B ”	2	“T _B ” (200 °C)
“S ₆ ”	“D _B ”	4	“T _A ” (1st cycle at 250 °C, 2nd cycle at 200 °C, and last two cycles at 150 °C)

and recrystallized grains are detectable, along with coarse ones from the previous microstructure. Since the second cycle, 200 °C processing with a total strain of 2.7 has led to a refined structure with a mean grain size of 6 μm; see Fig. 3(d). A more significant grain refinement of about 43% (mean grain size of 3.5 μm) was seen in the third cycle, processed at 150 °C with a

total strain of about 3.9; see Fig. 3(e). After the fourth cycle, 150 °C processing with a total strain of 5.2 led to further refinement with a mean grain size of 1.9 μm; see Fig. 3(f). The final microstructure is somewhat uniform, although some relatively large grains can still be detectable. Therefore, it can be said that the grain refinement after four CGP cycles through

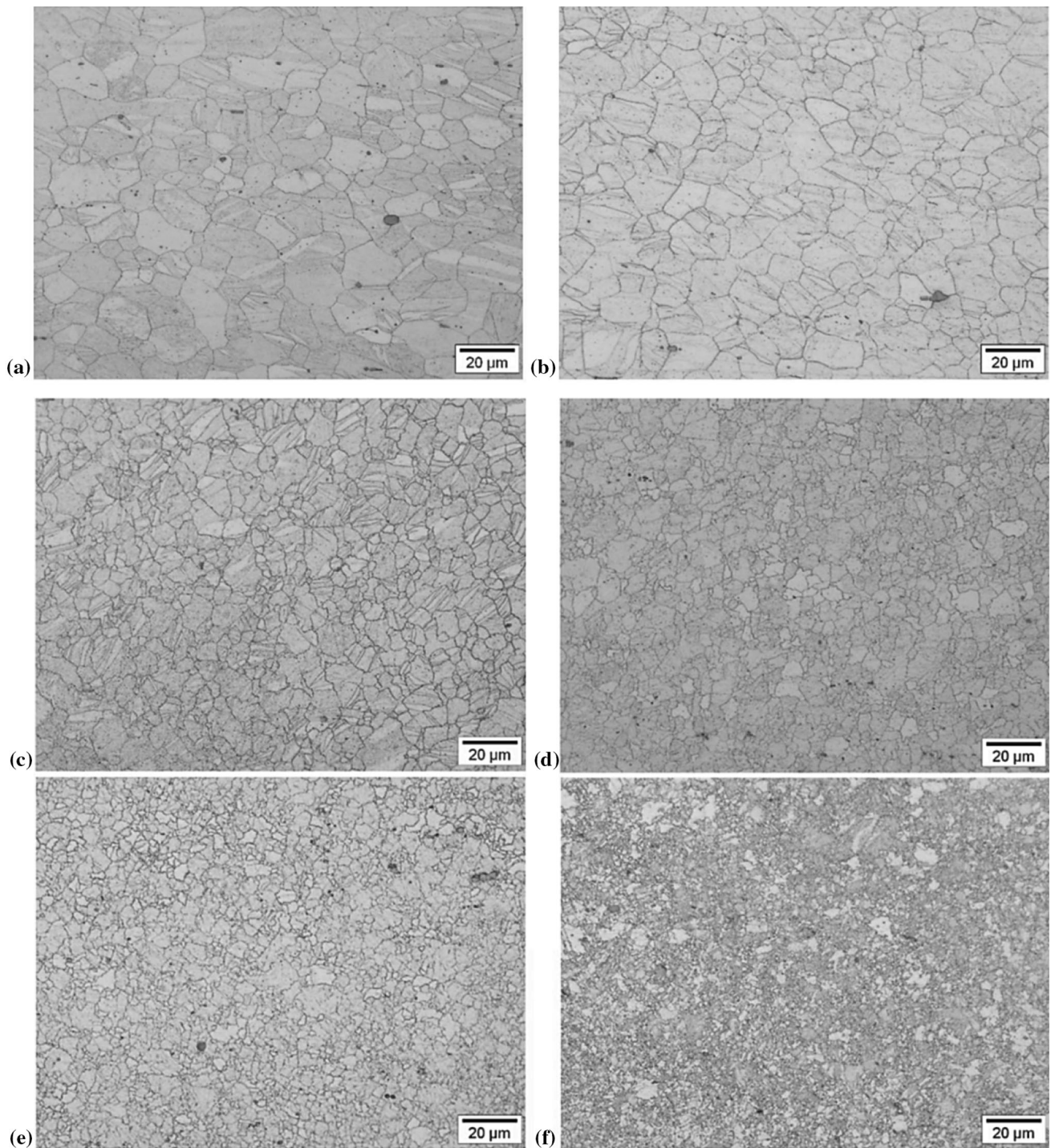


Fig. 3 Microstructure images of (a & b) initial annealed AZ31 alloy along the (a) rolling direction (RD) and (b) transversal direction (TD), and (c-f) sample “S₁” under the “D_A” and “T_A” procedure in the (c) first (d) second (e) third, and (f) fourth cycles

the “D_A” and “T_A” methods is about 85%. Therefore, it can be deduced that the efficiency of grain refinement in the mentioned process is acceptable if it is repeated until sufficient plastic strain is applied, hence this process is able to produce homogenous UFG structures in the whole sheet without fracture.

Figure 4 exhibits the microstructure of samples “S₁” to “S₆”. Also, Fig. 5 shows their mean grain size. Samples “S₂” to “S₄” were deformed with the identical “D_A” and “T_B”

procedures at temperatures ranging from 200 to 300 °C. The mean grain size of the “S₂” sample was about 3.8 μm, which is relatively coarse compared to sample “S₁” (mean grain size of 1.9 μm). In fact, increasing the deformation temperature has led to substantial grain coarsening, which is also evident in samples “S₃” and “S₄”, whose mean grain sizes were equal to 8.3 and 21.7 μm, respectively. The mean grain size of the “S₄” sample is coarser than that of the initial sample because of the high-temperature deformation, leading to substantial grain growth.

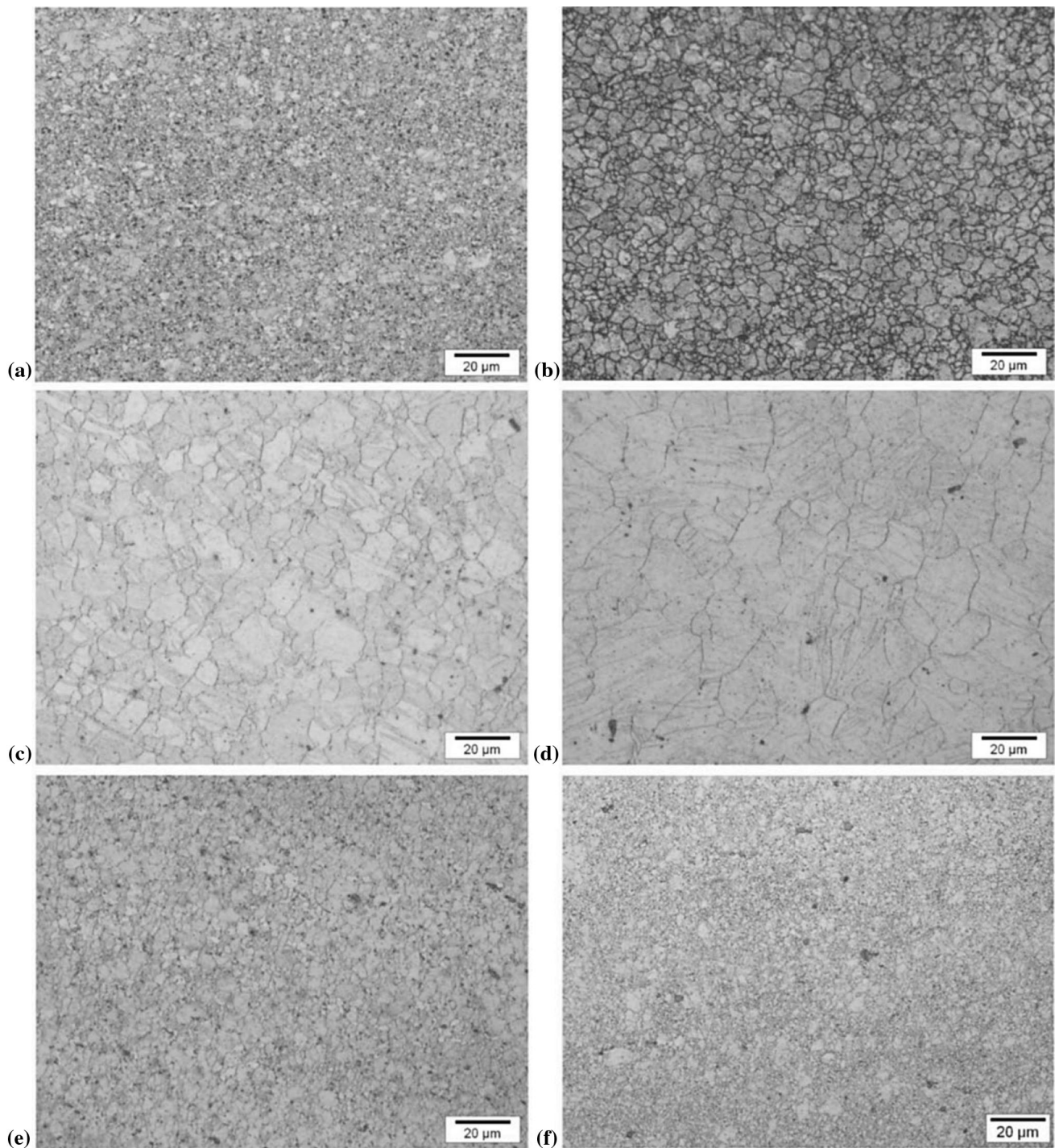


Fig. 4 Comparison of microstructure images in AZ31 alloy: (a) sample “S₁”, (b) sample “S₂”, (c) sample “S₃”, (d) sample “S₄”, (e) sample “S₅”, and (f) sample “S₆”

Both samples “S₂” and “S₅” were processed by means of the “T_B” method at a fixed temperature of 200 °C, but with distinct deformation successions of “D_A” and “D_B”, respectively. It is found that sample “S₅” has a smaller mean grain size (3.1 μm) than the “S₂” sample (3.8 μm). It is known that the refinement of grains depends on total strain. However, the “S₅” sample was deformed with a lower total strain (5) than the “S₂” sample (5.1), which manifests a lower mean grain size. However, the difference in strain or grain size is negligible; the deformation succession seems to play an essential role. The

grain size difference can be attributed to the difference in exposure time at high temperatures. This time varied due to differences in the number of required cycles in each deformation succession. The exposure time contains preheating, straining, and sample removal from the die. Samples “S₅” and “S₂” were repeatedly pressed 10 times in two cycles and 16 times in four cycles, respectively. In this way, the exposure time of sample “S₅” was shorter, and compared to sample “S₂”, it will have less chance for grain growth and recovery mechanisms in the preheating and post-deformation steps.

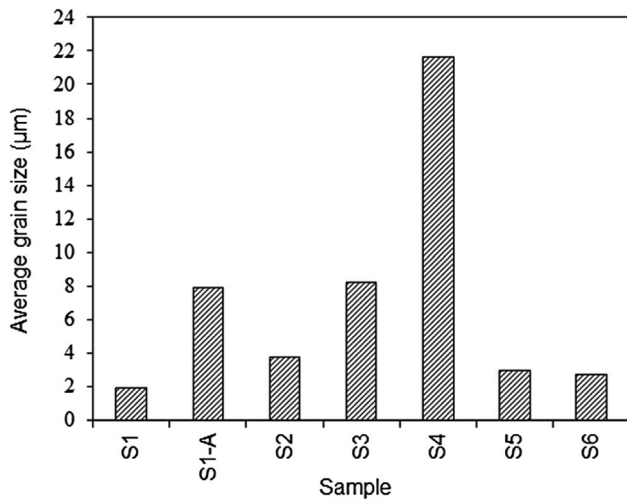


Fig. 5 Mean grain size in AZ31 samples of “S₁”, “S_{1-A}” (annealed), and “S₂” to “S₆”

From the comparison of sample “S₆” (“D_B” and “T_A” with a total strain of 9.8 after four cycles) and specimen “S₁” (“D_A” and “T_A” with a total strain of 5.3 after four cycles), it should be noted that the mean grain size in sample “S₆” (2.8 μm) is coarser than the “S₁” sample (1.9 μm). The mean grain size in sample “S₆”, in spite of its higher total strain than sample “S₁”, does not reduce remarkably, and this can be attributed to the long exposure time of the sample at high-temperature conditions. Sample “S₆” exposure duration at high temperature is longer since it requires more processing passes (20 times) than sample “S₁” (16 times), which provides more additional chances for grain growth. Note that sample “S₁” was annealed at 453 K for 1 hour in order to study the changes in ductility and strength. So, the mean grain size increased from 1.9 to 7.9 μm.

The microstructure observation of samples “S₁” to “S₆” indicates that it is readily possible to produce a fine microstructure in the CGP-processed AZ31 Mg sheet if appropriate processing conditions are considered. Indeed, if the temperature is kept below 250 °C, an adequately homogeneous fine microstructure can be obtained through a constant temperature (“T_B”) deformation method. Pressing at very high temperatures can lead to substantial grain coarsening because of the utilization of thermal energies at high magnitudes, providing the required driving force for the activation of grain boundary migration.

Microstructure evolution is most likely to be somewhat complicated because of the deformation and exposure duration of the sample in each processing stage. As it is known, the total time of exposure at high temperatures involves preheating, deformation, and right away following deformation. Amid preheating, the sample is continuously exposed to the opposing mechanisms between static recovery and recrystallization because of the accumulated energy induced in the earlier processing stage. Although dynamic recovery and dynamic recrystallization are the dominant mechanisms during plastic deformation, metadynamic recrystallization may also happen immediately after deformation. Previous studies (Ref 18, 63, 64) show that the partially dynamic recrystallized microstructure generally includes three regions: (1) dynamically recrystallized fine grains with no dislocations; (2) coarser

recrystallized grains with several dislocations; and (3) unre-crystallized grains with increased dislocation density. When the imposing strain is halted while the sample is still exposed to high temperatures, various modifications in the microstructural conditions may happen. In region (1), fine grains may continue to grow because of the annealing operation. Recovery or growth of recrystallization nuclei may appear in the region (2) if the dislocation density is lower than a critical amount. If this is higher than this critical magnitude, static recrystallization will proceed. Region (3) may experience static recovery, static recrystallization, and subsequent grain growth.

At higher temperatures, the grain growth kinetics increase in the preheating and post-deformation stages, so the grain refinement is intensified by dynamic recrystallization. This is obvious in the samples “S₃” and “S₆” deformed through the “T_B” method at temperatures of 250 and 300 °C, respectively, where substantial grain coarsening is detectable. The microstructure at 300 °C is mainly composed of large grains. Refined grains can be obtained in the “S₂” sample processed by the “T_B” method at 250 °C due to the higher dynamic recrystallization rate and minimal grain growth. Therefore, gradually reducing the processing temperature with the T_A method is a remarkably effective approach to achieving significantly fine-grain microstructures. Processing the sample at lower temperatures, such as 200 °C, is possible due to the improved workability of the material in terms of grain refinement in the previous cycles. Therefore, this leads to additional dislocation accumulation in the grains, enabling intensive grain refinement through the subdivision of grains using the continuous dynamic recrystallization phenomenon (Ref 17, 48). In addition, at lower deformation temperatures, the twin-induced grain refinement result may accelerate grain refinement [34, 105-107]. It should be noted that the interplay of twin boundaries and slip dislocations increments the nucleation sites, leading to the fabrication of finer dynamically recrystallized grains (Ref 65-67).

3.2 Texture Evolution

The pole figures of the initial AZ31 Mg alloy are shown in Fig. 6, which includes a strong basal texture {0002}. The alterations in the basal {0002}, prismatic {10-10}, and pyramidal {10-11} pole figures of the “S₁” sample after each cycle are shown in Fig. 7. It can be observed that with the advancement of the deformation cycle, the intensity of the basal texture is redistributed from ND to RD-TD. Meanwhile, the randomly distributed prismatic intensity around RD-TD is redistributed to the ND. Although the intensity of the basal texture gradually diminishes from the first to the third cycle, it shows a slight increase after the fourth cycle. The results indicate the generation of a fresh texture by applying the CGP technique, by which some grains tilt their c-axis in the hcp system from the normal direction to RD-TD. The observed texture alteration is due to shear deformation and the interplay between slips and twinning, leading to recrystallized grain fabrication with basal and non-basal orientations.

Figure 8 shows the final {0002}, {10-10}, and {10-11} pole figures in samples “S₁” to “S₆”. It should be noted that the mechanical properties and texture of sample “S₄” were not studied due to the substantial grain coarsening. Also, this work predominantly concentrates on the mechanical performance and texture of the grain-refined samples. From the “S_{1-A}” pole figures (after the annealing operation) in Fig. 8(a) and (b), the

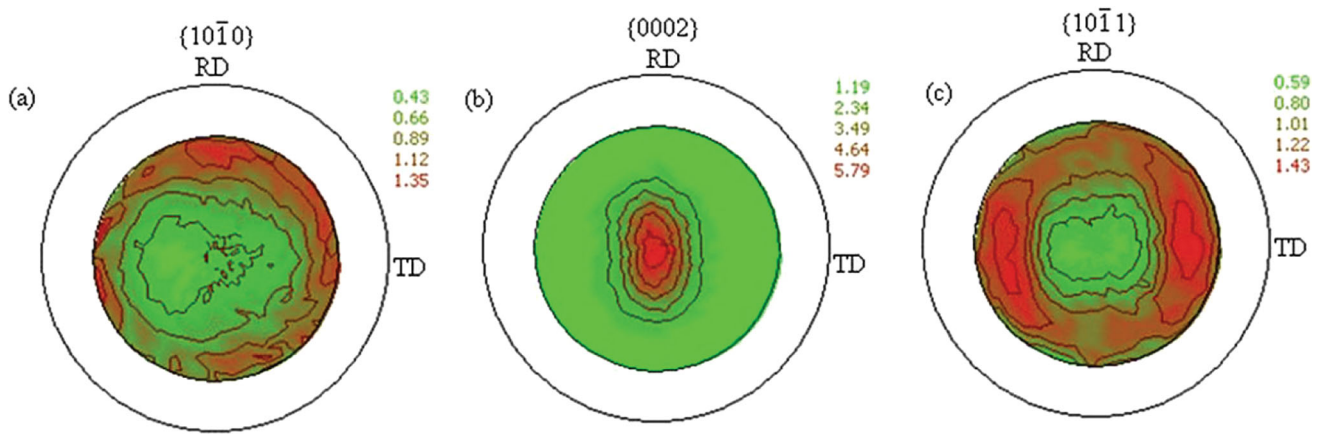


Fig. 6 The AZ31 Mg alloys' pole figure representation of the initial annealed sample: (a) prismatic, (b) basal, and (c) pyramidal

deformation texture is preserved to some extent. Although the intensity of the basal texture is marginally increased in the comparison “S₁” sample, it is still much lower than the initial material. Also, the basal intensity in the “S₆” sample (“D_B” and “T_A”) is strongly distributed in the central part of the pole figure, indicating a much higher intensity value than the initial sample. This could be due to the superior total strain and higher compressive and tensile stresses in the “D_B” procedure in comparison with the “D_A” process. According to a study in Ref. 37, the total strain in sample “S₆” compared to sample “S₁” is estimated to be about 9.9 and 5.2, respectively. Furthermore, the highest strain on the sample “S₆” is related to the last two cycles at a lower temperature of 200 °C. The compression processing along the ND of the sheet seems to stimulate grain extension twinning. Note that the c-axis is first away from the normal direction. In addition, the twinning occurrence can also lead to grain rotation so that their c-axis is aligned in a parallel manner to the loading direction. Consecutive tensile strain is accommodated over the RD-TD because of the stretching with basal slips that additionally reinforces basal texture (Ref 68, 69).

The pole figures of samples “S₂” and “S₆” are represented in Fig. 8(c) and (f), respectively. Note that each of the two samples was deformed with the quite same total strain value (5.1 in “S₂” and 5 in “S₅” condition) and “T_B” (at 200 °C) procedure, but under varied processing conditions. In comparison with “S₂”, which has a basal intensity of 3.9, sample “S₆” exhibits a lower basal intensity of 2.5. In addition, it was concluded that the texture in sample “S₅” is considerably more deficient than that in sample “S₆”. Both specimens were deformed by the same “D_B” procedure but with diverse thermal successions. The reason for the weaker basal texture of the “S₅” sample than the “S₆” sample is attributed to the different processing temperatures and the total strain. Sample “S₆”, which reached an elevated total strain at low temperature during the final two cycles, increased the twinning and basal slip actions, resulting in the intensification of the basal type of texture obtained.

3.3 Mechanical Behavior

Figure 9(a) displays the variation of hardness in each deformation step at the thickness of the “S₁” sample. It should be noted that the measurements were made from the top to the bottom of the sheet surface. The results indicate minimal

hardness variation, especially at higher cycles. This states that plastic strain is uniform at the higher deformation cycles. Figure 9(b) illustrates a diagram of the mean hardness along with mean grain size versus the strain value in the “S₁” sample during processing cycles. Based on these diagrams, the hardness variations after each cycle correspond well with the procedure of grain refinement. For instance, compared to the second cycle, the hardness after the third cycle increases strongly, which is consistent with the mean grain size reduction (43%) in the third cycle. It should be noted that the amount of accumulative plastic strain during the CGP process was calculated using Eq 1. In this relationship, N and θ are the pass number and groove angle, respectively.

$$\bar{\epsilon} = \frac{2N \tan \theta}{\sqrt{3}} \quad (\text{Eq 1})$$

Figure 10 illustrates the stress-strain trends of the “S₁” sample fabricated according to the “D_A” and “T_A” methods after each cycle of the CGP process. The analogy between the stress-strain trends of “S₁” and “S₆” specimens is exhibited in Fig. 11. For a better comparison, Fig. 12 indicates the magnitudes of yield strength (YS), ultimate tensile strength (UTS), and elongation-to-failure (EL) resulting from the true stress-strain plots. The results obtained in Fig. 10 show that with the increase in the CGP cycle, the strength of sample “S₁” increased while the elongation-to-failure decreased. The elongation-to-failure (15-23%) is maintained after the 2nd cycle due to the higher deformation temperature, which is related to the promotion of static recovery and static recrystallization. Also, the changes in YS, UTS, and EL of sample “S₁” after four cycles along the rolling direction are approximately 47, 1.7, and – 65% as opposed to the initial material. Following a one-hour annealing treatment of the sample “S₁” at 200 °C (“S_{1-A}” sample), the elongation-to-failure reaches about 20% compared to the initial sample. In addition, the YS and UTS decrease after annealing, which will be 12% more and 13% less than the initial sample, respectively. Therefore, the stress-strain condition of sample “S_{1-A}” in both rolling and transverse directions will be less anisotropic due to the annealing heat treatment.

According to Fig. 11, it can be recognized that the stress-strain diagrams in the rolling and transverse directions of samples “S₂” and “S₅” have greater inhomogeneity and anisotropy. In this regard, the elongation-to-failure in RD is considerably higher than in TD. Also, the increased ductility in

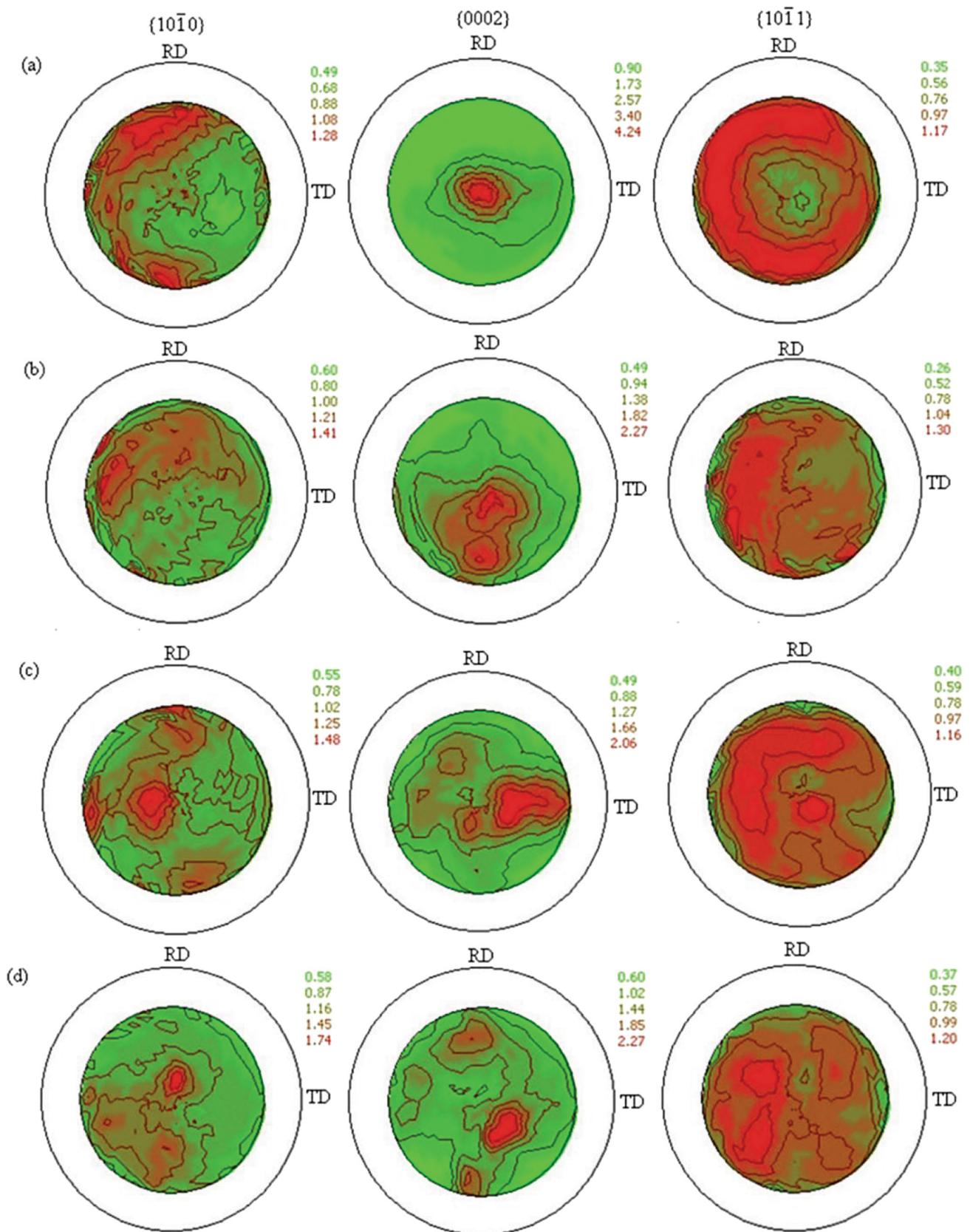


Fig. 7 The pole figures of “ D_A ” and “ T_A ” processed the “ S_1 ” sample following the (a-d) first to fourth cycles, respectively

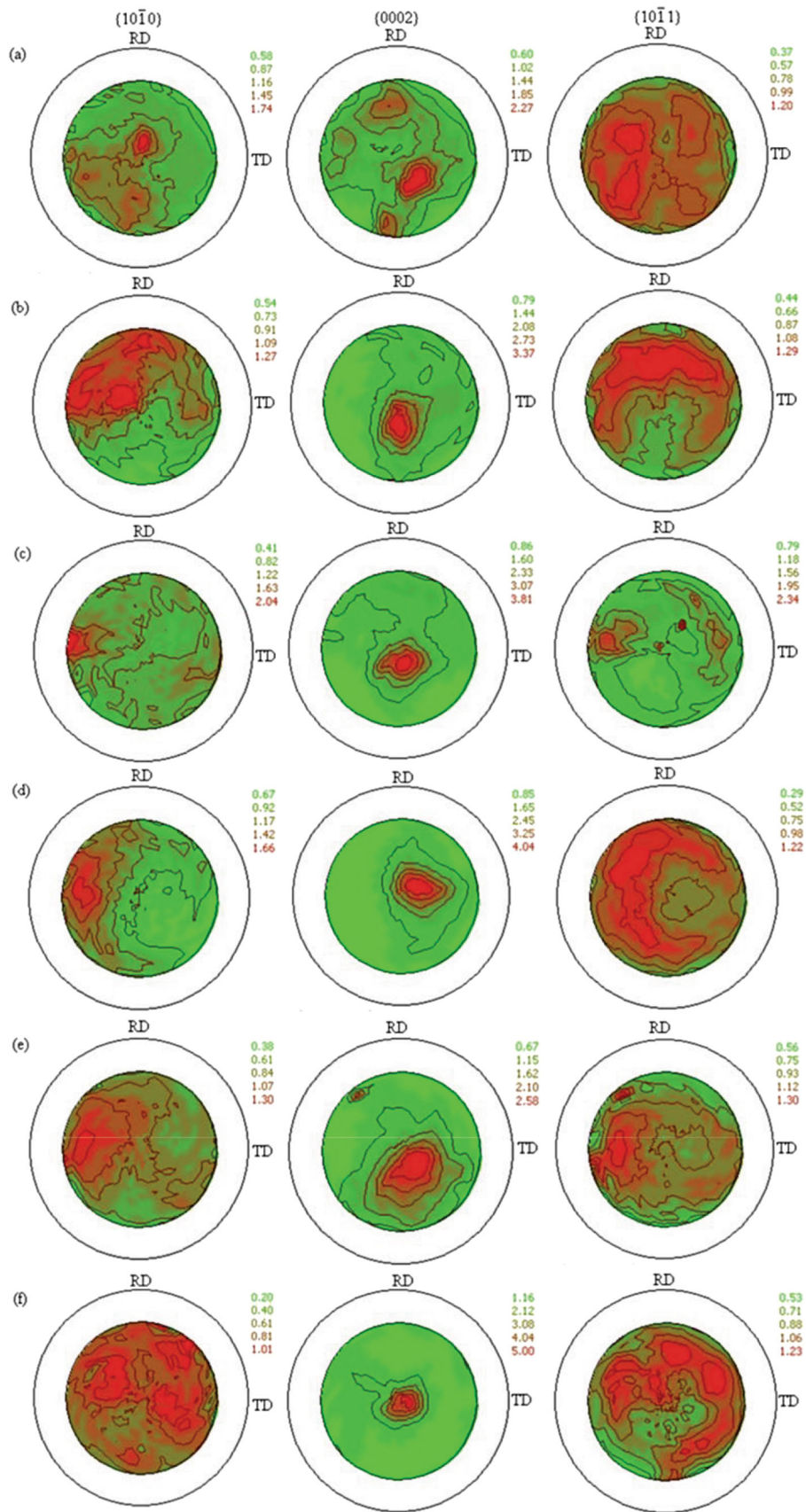


Fig. 8 The pole figures with basal, prismatic, and pyramidal types of the AZ31 magnesium alloy. Note that conditions “S₁”, “S_{1-A}”, “S₂”, “S₃”, “S₅”, and “S₆” are represented by (a) to (f), respectively

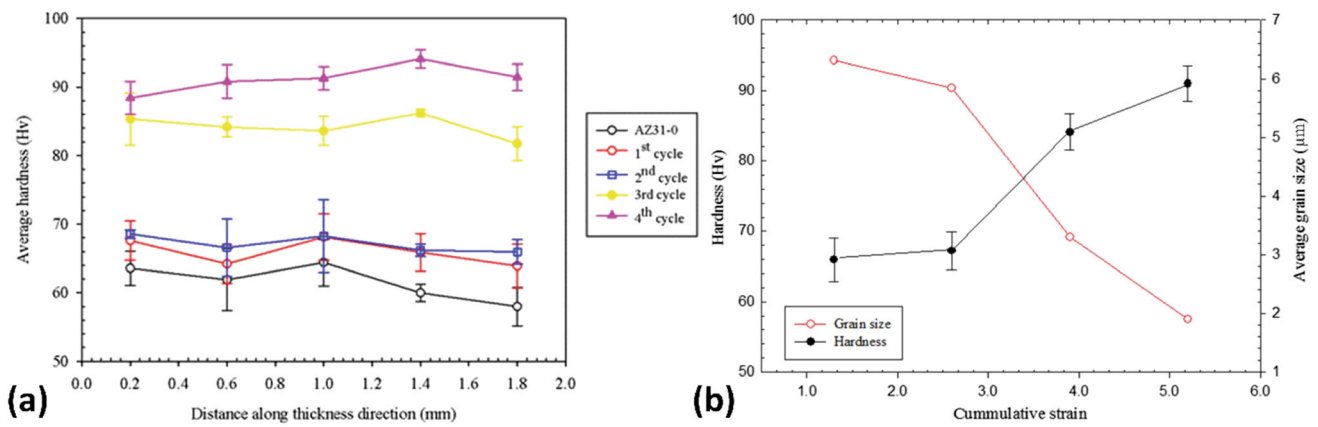


Fig. 9 (a) Alteration of hardness values in the thickness of sample “S₁” after different cycles of deformation processing and (b) mean hardness and mean grain size diagram in sample “S₁” following every cycle in terms of the total strain

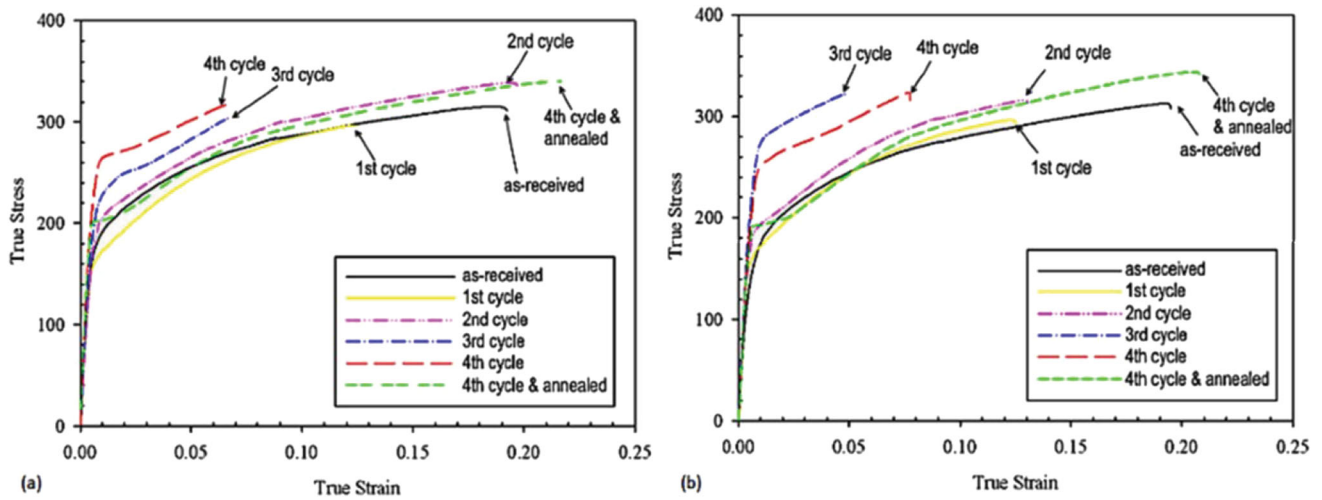


Fig. 10 The trend of true stress-strain values for the “S₁” sample following the first to fourth cycle and after four cycles with annealing operation versus the initial sample in two directions (a) rolling and (b) transverse

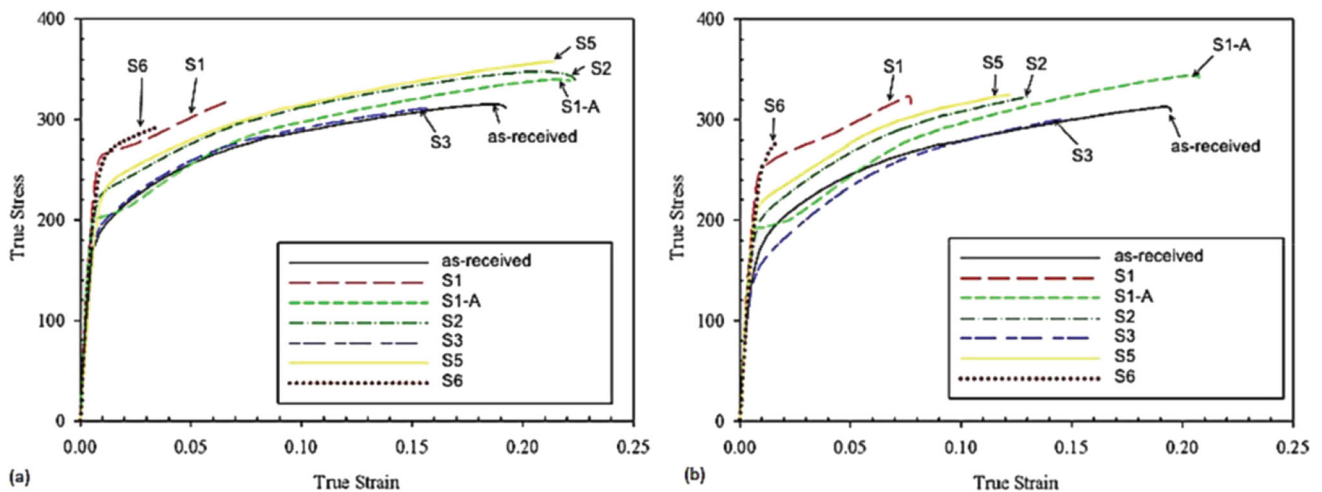


Fig. 11 True stress-strain curves for different samples of AZ31 Mg alloy in two directions: (a) rolling and (b) transverse

RD can be due to the texture evolution of these specimens, in which, according to Fig. 8, the basal intensities are redistributed towards RD compared to TD. This contributes to the additional

basal slip along the RD relative to the TD in the work-hardened materials (Ref 70). Additionally, the “S₂” sample exhibits increased yield strength and elongation-to-failure in compar-

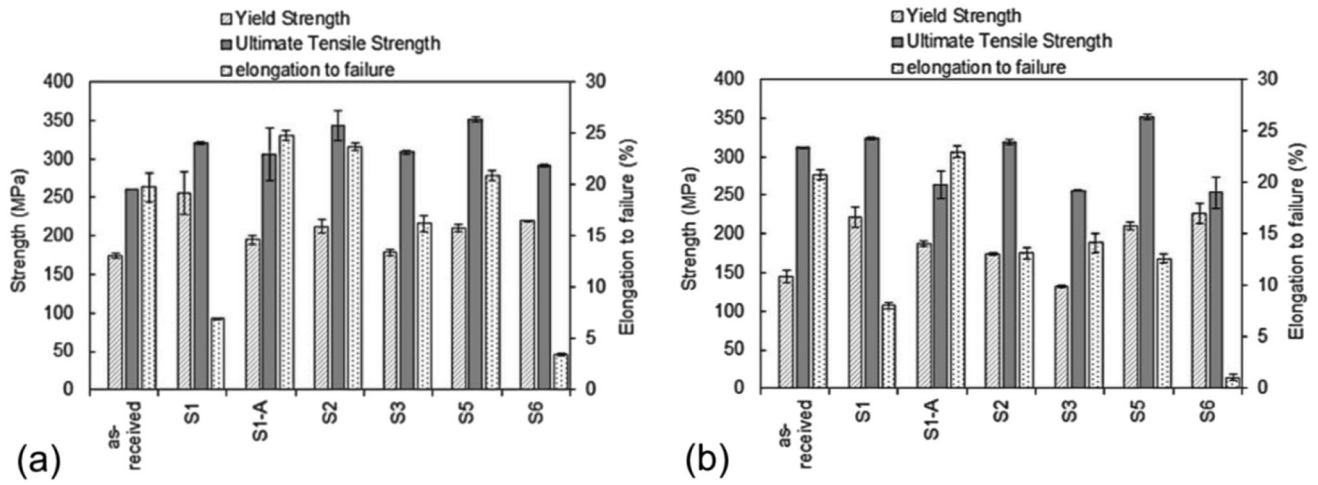


Fig. 12 Mechanical properties, including yield and ultimate tensile strength, along with elongation-to-failure in two directions: (a) rolling and (b) transverse for different samples

ison with the “S₃” sample. Indeed, the diminished strength and ductility in the “S₃” sample are because of its coarser grains. The YS and UTS, along with the El of the “S₂” sample, are approximately 22%, 9%, and 20% higher than the initial counterpart. So, samples “S_{1-A}” and “S₂” have better ductility because of their low textural strength, low work-hardening effect, and refined microstructure. In a study by Koike et al., fine grains increased the activity of non-basal slips (71).

Another noteworthy point considering the stress-strain plots in Fig. 11 and 12 is the incidence of yield point elongation in the four-cycle and the annealed samples. This implies that the stress-strain plot has a slight plateau that extends beyond yielding. Such a circumstance is related to stress relaxation at the twins’ tips when they meet the grain boundaries and propagate in the subsequent grains (Ref 72). Based on the examination of the twins per grain number in the fine-grained Mg alloy, the fabrication of nearly one twin per grain is a prerequisite for yield point elongation (Ref 72). It essentially allows twins to propagate throughout the grain, stop at the boundaries of the grain, and advance toward the adjacent grain by re-initiation or propagation. Such a possibility does not exist in structures with coarse grains since there are more twins per grain, increasing the probability of their impingement with each other.

Figure 13 represents the SEM observation of the fracture morphology of the tensile samples deformed in the “S₁” condition in both rolling and transverse directions. The fracture surfaces mainly have dimple structures in the as-received samples for both rolling and transverse directions (Fig. 13a-d). These dimples are deep and wide because of the grain growth during heat treatment. This is since the voids nucleate at the boundaries of larger grains, where they subsequently coalesce and grow. Following the first cycle, the fracture surface of the “S₁” sample exhibits a greater number of equiaxed and oval-shaped dimples with a small fraction of the sheared surfaces in both studied orientations; see Fig. 13e-h. In addition, some enlarged dimple holes can be detected in these tested samples. A small fraction of dimples with different sizes and depths can be observed on the fractured surface of the “S₁” sample, which was evaluated after the fourth cycle (Fig. 13i-j). There are some cleavage facets stretched longitudinally in some relatively flat regions with little dimples. The sample has a shear failure,

which is indicative of the ductile-brittle fracture mode typically observed in Mg alloys with medium ductility at ambient temperature. The findings demonstrate that as CGP cycle numbers increase, the failure mode changes from ductile to ductile-brittle.

To examine the mechanical inhomogeneity and anisotropy in the CGP-processed sheets, plastic strain ratio, normal and planar anisotropies (*r*-value, *r_m*, and Δ*r*) were utilized after the tensile tests at ambient temperature. A previous study showed that the uniform elongation in Mg alloys is up to 10% (Ref 62). Also, the *r*-value changes a little with the tensile elongation. Consequently, for this work, the *r*-value was considered at an engineering strain of 8% in the tensile direction. The plastic strain ratio, which is calculated using strain values at an engineering strain of 8%, is used to determine the anisotropy degree between the in-plane and through the thickness. In this regard, Eq 2 is used to derive the *r*-values in rolling, 45°, and transverse directions, where ϵ_l , ϵ_t , and ϵ_w represent the amount of plastic strain in the length, thickness, and width directions at an 8% engineering tensile strain, respectively (Ref 73). In addition, the normal anisotropy (also called average strain ratio) is calculated through Eq 3, where r_0 , r_{45} , and r_{90} represent the *r*-values achieved in the rolling, 45°, and transverse orientations, respectively. Furthermore, planar anisotropy is calculated through Eq 4 in order to determine the material uniformity during the drawing operation (Ref 74). In this regard, Tables 3 and 4 compare the tensile response and mechanical anisotropy of AZ31 Mg alloys in several deformation steps, respectively.

$$r\text{-value} = \frac{\epsilon_w}{\epsilon_t} = \frac{\epsilon_w}{-(\epsilon_l + \epsilon_w)} \quad (\text{Eq 2})$$

$$r_m = \frac{r_0 + 2r_{45} + r_{90}}{4} \quad (\text{Eq 3})$$

$$r = \frac{r_0 - 2r_{45} + r_{90}}{2} \quad (\text{Eq 4})$$

According to Table 3, the annealed CGP sheet along the rolling direction shows a substantial improvement in mechanical strength and ductility in comparison with the existing products with fully annealed and rolled sheets. Meanwhile, the mechanical performance of the annealed processed sheet in the

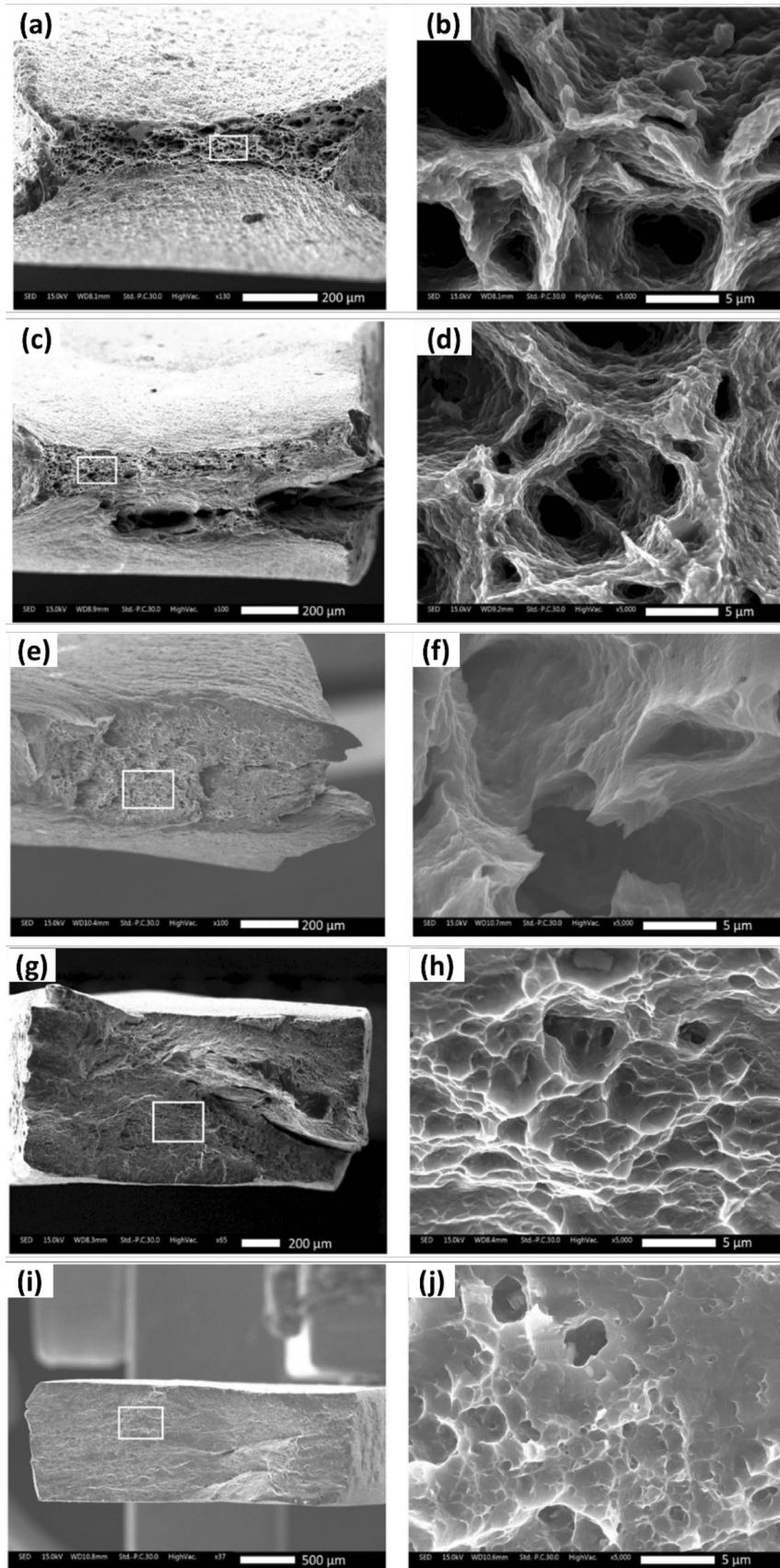


Fig. 13 Fracture morphology of tensile AZ31 Mg alloy: (a-d) as-received sample, (e-h) “S₁” sample after the first cycle, and (i-j) “S₁” sample after the fourth cycle. Note that (a), (c), (e), (g), (i) and (b), (d), (f), (h), (j) correspond to the rolling and transverse directions, respectively

Table 3 An overview of tensile properties for the AZ31 Mg alloy under different deformation processes of the CGP technology

Processing conditions	Yield strength, MPa			Ultimate tensile strength, MPa			Elongation-to-failure, %		
	RD	45°	TD	RD	45°	TD	RD	45°	TD
Normal rolling of the hot-extruded sheet (Ref 75)	166.4	166.4	171.2	256.6	254.9	254.9	22.8	21.8	21.1
Differential speed rolling of the hot-extruded sheet (Ref 75)	145.5	158.9	176.0	259.2	258.5	259.2	25.5	24.6	23.1
As-rolled sheet (Ref 62)	163	175	186	263	263	275	16	19	17
Annealed sheet (this case)	172.0	143.0	138.0	259.7	197.3	248.4	19.0	20.0	22.3
CGP-processed sample, “S _{1-A} ” (this case)	191.5	165.0	174.9	266.3	173.7	264.5	23.4	13.3	21.7

Table 4 The corresponding plastic strain ratio, normal and planar anisotropies for Mg alloy during various deformation states of the CGP process

Processing state	Plastic strain ratio			Normal anisotropy	Planar anisotropy
	RD	45°	TD		
Rolling (normal type) of the extruded sheet (Ref 75)	2.98	3.10	3.39	3.151	0.12
Rolling (differential speed type) of the extruded sheet (Ref 75)	1.85	2.47	3.27	2.515	0.09
As-rolled sheet (Ref 62)	1.92	2.11	2.92	2.27	0.3
Annealed sheet (this study)	1.49	1.23	0.94	1.2	- 0.02
CGP-processed sample, “S _{1-A} ” (this study)	1.37	1.53	1.02	1.4	- 0.3

transverse direction is quite proportionate to that of the sheets. In this regard, the ductility of the annealed CGP sheet in the 45° direction is lower than in other directions of the material. This increase in anisotropy can be attributed to the grains' alignment towards both RD and TD, deduced from the pole figure in Fig. 8(b), and is related to the CGP pressing strategy (180/90° sample rotation). This kind of alignment in grains favors < a > type dislocation slip at ambient temperature tensile deformation. The processed specimen has improved strength properties but better ductility along the rolling direction as compared to conventional rolling and differential speed rolling of the hot-extruded sheets. Additionally, the mechanical performance is very similar in the transverse direction but reduced considerably in the 45° direction.

It is necessary to clarify that the normal and planar anisotropy were estimated based on the plastic strain ratio to further analyze the sheet metal formability. For this aim, plastic strain ratios have been calculated based on the 8% engineering strain in Mg alloys (Ref 62). It is generally accepted for cubic structures that a higher *r*-value manifests superior formability (Ref 72, 76). Nevertheless, the interpretation of the *r*-value for hexagonal alloys is reversed. From deep drawing experiments with various Mg alloys, it was found that a higher *r*-value is related to less drawability (Ref 62). It means an elevated *r*-value indicates more mechanical anisotropy and less formability. Based on Table 4, the *r*-value of the annealing processed sheet along the 45° direction is the maximum value compared to rolling and transverse directions, which is due to its low ductility. Also, the annealed CGP sheet has a lower value of *r_m* compared to the rolled sheet and slightly higher compared to the annealed sheet. Note that the value of Δr in the annealed CGP sheet is more negative than the other materials, indicating that it is more susceptible to fracture in the 45° loading

direction. In general, the values of *r* and *r_m* at the annealed processed sheet are further reduced than the conventional rolling and differential speed rolling of the extruded sheet, indicating the superior formability of the deformed alloy. The Δr value in the rolled sheet is maximal, which implies that the material may draw nonuniformly during the deep drawing process (Ref 76, 77).

4. Conclusions

- Introducing sample rotation during deformation cycles using “D_A” or “D_B” deformation succession and gradual temperature reduction through the “T_A” method is an efficacious procedure to produce homogenous fine- to ultra-fine-grained microstructure in Mg sheets. In this regard, the sample subjected to “D_A” and “T_A” leads to an improvement of 48.6% and 1.7%, respectively, in the yield and ultimate tensile strength as opposed to the initial sample, while the elongation-to-failure decreases by about 64.8%. After one-hour annealing treatment at 200 °C, the YS and UTS, along with El, changed by roughly 12-13%, and 20% in comparison with the initial sample.
- “D_B” deformation succession is more efficacious because a smaller number of pressings are required to attain the same magnitude of total strain. Also, samples processed by D_B and “T_A” reached a comparable magnitude of grain refinement in comparison with “D_A” and “T_A”.
- Basal texture weakening was detected during each CGP step in the “S₁” sample. In “S₁” to “S₅” specimens, the basal intensities were rearranged from the ND toward the RD-TD, whereas the pyramidal and prismatic intensities, which were originally irregularly adjusted about the RD-

TD, approached the ND direction. The basal intensities and, consequently, the strength of the texture after the process decreased compared to the initial sample.

- The basal strength of the “S₆” sample is increased in comparison with the initial sample due to the application of a high amount of plastic strain, especially when most of the total strain was applied at the low-temperature deformation (200 °C) in the final two cycles.
- The mechanical anisotropy was determined in the annealing-deformed sheet. Normal anisotropy values, from the highest to the lowest ranking, are conventional rolling of a hot-extruded sheet, differential speed rolling of a hot-extruded sheet, rolled sheet, and annealed CGP sheet. In general, a lower normal anisotropy value indicates better formability of the Mg sheet. Also, the planar anisotropy values from the highest to the lowest ranking are rolled sheet, conventional rolling of the hot-extruded sheet, differential speed rolling of a hot-extruded sheet, and annealed CGP sheet. Further positive planar anisotropy magnitude indicates more inhomogeneous draw-in during deep drawing, whereas a further negative magnitude means more susceptibility to sheet fracture in the 45° direction.

Acknowledgment

This work was financially supported by the Xuzhou Urbanization Renju Environment Design Engineering Technology Research Center of China.

Conflict of interest

The authors declare no conflict of interest.

References

1. B. Xie, H. Li, Y. Ning, and M. Fu, Discontinuous Dynamic Recrystallization and Nucleation Mechanisms Associated with 2-, 3- and 4-Grain Junctions of Polycrystalline Nickel-Based Superalloys, *Mater. Des.*, 2023, **231**, p 112041. <https://doi.org/10.1016/j.matdes.2023.112041>
2. L. Chen, Y. Zhao, M. Li, L. Li, L. Hou, and H. Hou, Reinforced AZ91D Magnesium Alloy with Thixomolding Process Facilitated Dispersion of Graphene Nanoplatelets and Enhanced Interfacial Interactions, *Mater. Sci. Eng. A*, 2021, **804**, p 140793. <https://doi.org/10.1016/j.msea.2021.140793>
3. W. Liu, Y. Zhao, Y. Zhang, C. Shuai, L. Chen, Z. Huang, and H. Hou, Deformation-Induced Dynamic Precipitation of 14H-LPSO Structure and Its Effect on Dynamic Recrystallization in Hot-Extruded Mg-Y-Zn Alloys, *Int. J. Plast.*, 2023, **164**, p 103573. <https://doi.org/10.1016/j.ijplas.2023.103573>
4. M. Li, Q. Guo, L. Chen, L. Li, H. Hou, and Y. Zhao, Microstructure and Properties of Graphene Nanoplatelets Reinforced AZ91D Matrix Composites Prepared by Electromagnetic Stirring Casting, *J. Mater. Res. Technol.*, 2022, **21**, p 4138–4150. <https://doi.org/10.1016/j.jmrt.2022.11.033>
5. L. Chen, Y. Zhao, J. Jing, and H. Hou, Microstructural Evolution in Graphene Nanoplatelets Reinforced Magnesium Matrix Composites fabricated Through Thixomolding Process, *J. Alloys Compd.*, 2023, **940**, p 168824. <https://doi.org/10.1016/j.jallcom.2023.168824>
6. Y.V.R.K. Prasad, and K.P. Rao, Processing Maps for Hot Deformation of Rolled AZ31 Magnesium Alloy Plate: Anisotropy of Hot Workability, *Mater. Sci. Eng. A*, 2008, **487**, p 316–327. <https://doi.org/10.1016/j.msea.2007.10.038>
7. J. Hirsch and T. Al-Samman, Superior Light Metals by Texture Engineering: Optimized Aluminum and Magnesium Alloys for Automotive Applications, *Acta Mater.*, 2013, **61**, p 818–843. <https://doi.org/10.1016/j.actamat.2012.10.044>
8. G. Martin, C.W. Sinclair, and J.-H. Schmitt, Plastic Strain Heterogeneities in an Mg–1Zn–0.5Nd Alloy, *Scr. Mater.*, 2013, **68**, p 695–698. <https://doi.org/10.1016/j.scriptamat.2013.01.017>
9. T. Dessolier, P. Lhuissier, F. Roussel-Dherbey, F. Charlot, C. Josserond, J.-J. Blandin, and G. Martin, Effect of Temperature on Deformation Mechanisms of AZ31 Mg-Alloy under Tensile Loading, *Mater. Sci. Eng. A*, 2020, **775**, p 138957. <https://doi.org/10.1016/j.msea.2020.138957>
10. C.C. Aydiner and M.A. Telemez, Multiscale Deformation Heterogeneity in Twinning Magnesium Investigated with In Situ Image Correlation, *Int. J. Plast.*, 2014, **56**, p 203–218. <https://doi.org/10.1016/j.ijplas.2013.12.001>
11. D. Liao, S.-P. Zhu, B. Keshtegar, G. Qian, and Q. Wang, Probabilistic Framework for Fatigue Life Assessment of Notched Components Under Size Effects, *Int. J. Mech. Sci.*, 2020, **181**, p 105685. <https://doi.org/10.1016/j.ijmecsci.2020.105685>
12. X. Niu, S.-P. Zhu, J.-C. He, D. Liao, J.A.F.O. Correia, F. Berto, and Q. Wang, Defect Tolerant Fatigue Assessment of AM Materials: Size Effect and Probabilistic Prospects, *Int. J. Fatigue*, 2022, **160**, p 106884. <https://doi.org/10.1016/j.ijfatigue.2022.106884>
13. X.-K. Li, S.-P. Zhu, D. Liao, J.A.F.O. Correia, F. Berto, and Q. Wang, Probabilistic Fatigue Modelling of Metallic Materials Under Notch and Size Effect using the Weakest Link Theory, *Int. J. Fatigue*, 2022, **159**, p 106788. <https://doi.org/10.1016/j.ijfatigue.2022.106788>
14. P. Zhao, J. Zhu, K. Yang, M. Li, G. Shao, H. Lu, Z. Ma, H. Wang, and J. He, Outstanding Wear Resistance of Plasma Sprayed High-Entropy monoboride Composite Coating by Inducing Phase Structural Cooperative Mechanism, *Appl. Surf. Sci.*, 2023, **616**, p 156516. <https://doi.org/10.1016/j.apsusc.2023.156516>
15. W.P. Jia, X.D. Hu, H.Y. Zhao, D.Y. Ju, and D.L. Chen, Texture Evolution of AZ31 Magnesium Alloy Sheets During Warm Rolling, *J. Alloys Compd.*, 2015, **645**, p 70–77. <https://doi.org/10.1016/j.jallcom.2015.04.121>
16. B. Wang, L. Deng, C. Adrien, N. Guo, Z. Xu, and Q. Li, Relationship Between Textures and Deformation Modes in Mg–3Al–1Zn Alloy During Uniaxial Tension, *Mater. Charact.*, 2015, **108**, p 42–50. <https://doi.org/10.1016/j.matchar.2015.08.014>
17. T. Sakai, A. Belyakov, R. Kaibyshev, H. Miura, and J.J. Jonas, Dynamic and Post-dynamic Recrystallization Under Hot, Cold and Severe Plastic Deformation Conditions, *Prog. Mater. Sci.*, 2014, **60**, p 130–207. <https://doi.org/10.1016/j.pmatsci.2013.09.002>
18. M. Ebrahimi, Q. Wang, and S. Attarilar, A Comprehensive Review of Magnesium-Based Alloys and Composites Processed by Cyclic Extrusion Compression and the Related Techniques, *Prog. Mater. Sci.*, 2023, **131**, p 101016. <https://doi.org/10.1016/j.pmatsci.2022.101016>
19. M. Ebrahimi and M.A. Par, Twenty-Year Uninterrupted Endeavor of Friction Stir Processing by Focusing on Copper and Its Alloys, *J. Alloys Compd.*, 2019, **781**, p 1074–1090. <https://doi.org/10.1016/j.jallcom.2018.12.083>
20. F. Djavaanroodi, M. Ebrahimi, B. Rajabifar, and S. Akramzadeh, Fatigue Design Factors for ECAPed Materials, *Mater. Sci. Eng. A*, 2010 <https://doi.org/10.1016/j.msea.2010.09.080>
21. P. Fernandez-Zelaia and S.N. Melkote, Process–Structure–Property Relationships in Bimodal Machined Microstructures Using Robust Structure Descriptors, *J. Mater. Process. Technol.*, 2019, **273**, p 116251. <https://doi.org/10.1016/j.jmatprotec.2019.116251>
22. M. Ebrahimi and C. Gode, Severely Deformed Copper by Equal Channel Angular Pressing, *Prog. Nat. Sci. Mater. Int.*, 2017, **27**, p 244–250. <https://doi.org/10.1016/j.pnsc.2017.03.002>
23. R. Valiev, Nanostructuring of Metallic Materials by SPD Processing for Advanced Properties, *Nat. Mater.*, 2004, **3**, p 511–516. <https://doi.org/10.1039/146.110095>
24. R.Z. Valiev and T.G. Langdon, Principles of Equal-Channel Angular Pressing as a Processing Tool for Grain Refinement, *Prog. Mater. Sci.*, 2006, **51**, p 881–981. <https://doi.org/10.1016/j.pmatsci.2006.02.003>
25. W. Guo, Q. Wang, B. Ye, X. Li, X. Liu, and H. Zhou, Microstructural Refinement and Homogenization of Mg–SiC Nanocomposites by Cyclic Extrusion Compression, *Mater. Sci. Eng. A*, 2012, **556**, p 267–270. <https://doi.org/10.1016/j.msea.2012.06.086>

26. P. Luo, D.T. McDonald, W. Xu, S. Palanisamy, M.S. Dargusch, and K. Xia, A Modified Hall–Petch Relationship in Ultrafine-Grained Titanium Recycled from Chips by Equal Channel Angular Pressing, *Scr. Mater.*, 2012, **66**, p 785–788. <https://doi.org/10.1016/j.scriptamat.2012.02.008>
27. C. Yuhua, M. Yuqing, L. Weiwei, and H. Peng, Investigation of Welding Crack in Micro Laser Welded NiTiNb Shape Memory Alloy and Ti6Al4V Alloy Dissimilar Metals Joints, *Opt. Laser Technol.*, 2017, **91**, p 197–202. <https://doi.org/10.1016/j.optlastec.2016.12.028>
28. J. Xie, Y. Chen, L. Yin, T. Zhang, S. Wang, and L. Wang, Microstructure and Mechanical Properties of Ultrasonic Spot Welding TiNi/Ti6Al4V Dissimilar Materials Using Pure Al Coating, *J. Manuf. Process.*, 2021, **64**, p 473–480. <https://doi.org/10.1016/j.jmapro.2021.02.009>
29. M.H. Shaeri, M. Shaeri, M. Ebrahimi, M.T. Salehi, and S.H. Seyyedein, Effect of ECAP Temperature on Microstructure and Mechanical Properties of Al-Zn-Mg-Cu Alloy, *Prog. Nat. Sci. Mater. Int.*, 2016 <https://doi.org/10.1016/j.pnsc.2016.03.003>
30. M. Ebrahimi, S.A.N. Tiji, and F. Djavanroodi, Upper Bound Solution of Equal Channel Forward Extrusion Process as a New Severe Plastic Deformation Method, *Metall. Res. Technol.*, 2015 <https://doi.org/10.1051/etal/2015044>
31. M.M. Abramova, N.A. Enikeev, R.Z. Valiev, A. Etienne, B. Radiguet, Y. Ivanisenko, and X. Sauvage, Grain Boundary Segregation Induced Strengthening of an Ultrafine-Grained Austenitic Stainless Steel, *Mater. Lett.*, 2014, **136**, p 349–352. <https://doi.org/10.1016/j.matlet.2014.07.188>
32. F. Djavanroodi, M. Ebrahimi, and J.F. Nayfeh, Tribological and Mechanical Investigation of Multi-directional Forged Nickel, *Sci. Rep.*, 2019 <https://doi.org/10.1038/s41598-018-36584-w>
33. M. Ebrahimi and Q. Wang, Accumulative Roll-Bonding of Aluminum Alloys and Composites: An Overview of Properties and Performance, *J. Mater. Res. Technol.*, 2022, **19**, p 4381–4403. <https://doi.org/10.1016/j.jmrt.2022.06.175>
34. R.J. Fan, S. Attarilar, M. Shamsborhan, M. Ebrahimi, C. Göde, and H.V. Özkavak, Enhancing Mechanical Properties and Corrosion Performance of AA6063 Aluminum Alloys Through Constrained Groove Pressing technique, *Trans. Nonferrous Met. Soc. China*, 2020, **30**, p 1790–1802. [https://doi.org/10.1016/S1003-6326\(20\)65339-0](https://doi.org/10.1016/S1003-6326(20)65339-0)
35. M. Ebrahimi, Fatigue Behaviors of Materials Processed by Planar Twist Extrusion, *Metall. Mater. Trans. A Phys. Metall. Mater. Sci.*, 2017 <https://doi.org/10.1007/s11661-017-4375-4>
36. D.H. Shin, J.-J. Park, Y.-S. Kim, and K.-T. Park, Constrained Groove Pressing and Its Application to Grain Refinement of Aluminum, *Mater. Sci. Eng. A*, 2002, **328**, p 98–103. [https://doi.org/10.1016/S0921-5093\(01\)01665-3](https://doi.org/10.1016/S0921-5093(01)01665-3)
37. M. Ebrahimi, S. Attarilar, F. Djavanroodi, C. Gode, and H.S. Kim, Wear Properties of Brass Samples Subjected to Constrained Groove Pressing Process, *Mater. Des.*, 2014, **63**, p 531–537. <https://doi.org/10.1016/j.matdes.2014.06.043>
38. A. Sajadi, M. Ebrahimi, and F. Djavanroodi, Experimental and Numerical Investigation of Al Properties Fabricated by CGP Process, *Mater. Sci. Eng. A*, 2012 <https://doi.org/10.1016/j.msea.2012.04.121>
39. A.K. Gupta, T.S. Maddukuri, and S.K. Singh, Constrained Groove Pressing for Sheet Metal Processing, *Prog. Mater. Sci.*, 2016, **84**, p 403–462. <https://doi.org/10.1016/j.pmatsci.2016.09.008>
40. J.X. Fang, S.Y. Dong, S.B. Li, Y.J. Wang, B.S. Xu, J. Li, B. Liu, and Y.L. Jiang, Direct Laser Deposition as Repair Technology for a Low Transformation Temperature Alloy: Microstructure, Residual Stress, and Properties, *Mater. Sci. Eng. A*, 2019, **748**, p 119–127. <https://doi.org/10.1016/j.msea.2019.01.072>
41. J.X. Fang, J.X. Wang, Y.J. Wang, H.T. He, D.B. Zhang, and Y. Cao, Microstructure Evolution and Deformation Behavior During Stretching of a Compositionally Inhomogeneous TWIP-TRIP Cantor-Like Alloy by Laser Powder deposition, *Mater. Sci. Eng. A*, 2022, **847**, p 143319. <https://doi.org/10.1016/j.msea.2022.143319>
42. F. Fereshteh-Saniee, S. Ghorbanhosseini, and A. Sonboli, Inclusive Anisotropy and Texture Analyses of AZ91 Mg Sheets Subjected to Various Passes of Elevated-Temperature Constrained Groove Pressing, *Proc. Inst. Mech Eng. Part L J. Mater. Des. Appl.*, 2023, **237**, p 1638–1650. <https://doi.org/10.1177/14644207231152141>
43. G. Wang and L. Zhu, The Fracture Behavior and Thermal Stability of Commercially Pure Nickel Sheets Processed by Constrained Groove Pressing, *Metals (Basel)*, 2019, **9**, p 1047. <https://doi.org/10.3390/met9101047>
44. M. Akhil Sharma, C. Shravan Kumar, M. Nithin Kunal Reddy, and B. Tanya, Study on Mechanical Properties of AZ31-Mg Alloy and Effect of Deformation Using Constrained Groove Pressing—A Review Paper, *Mater. Today Proc.*, 2022, **62**, p 4463–4468. <https://doi.org/10.1016/j.matpr.2022.04.935>
45. S. Sama, S. Babbepalli, A. Budime, and T. Buddi, The Study of Mechanical and Microstructural Properties of the AZ31 Magnesium Alloy Using Constrained Groove Pressing at Elevated Temperature: A Review, *Mater. Today Proc.*, 2022, **62**, p 3429–3434. <https://doi.org/10.1016/j.matpr.2022.04.275>
46. S. Kumar, Developing Methods of Constrained Groove Pressing Technique: A Review, *Proc. Inst. Mech Eng. Part L J. Mater. Des. Appl.*, 2023, **237**, p 1319–1346. <https://doi.org/10.1177/1464420722143358>
47. Z. Wang, Y. Guan, T. Wang, Q. Zhang, X. Wei, X. Fang, G. Zhu, and S. Gao, Microstructure and Mechanical Properties of AZ31 Magnesium Alloy Sheets Processed by Constrained Groove Pressing, *Mater. Sci. Eng. A*, 2019, **745**, p 450–459. <https://doi.org/10.1016/j.msea.2019.01.006>
48. Q. Yang and A.K. Ghosh, Production of Ultrafine-Grain Microstructure in Mg Alloy by Alternate Biaxial Reverse Corrugation, *Acta Mater.*, 2006, **54**, p 5147–5158. <https://doi.org/10.1016/j.actamat.2006.06.045>
49. Q. Huo, X. Yang, H. Sun, B. Li, J. Qin, J. Wang, and J. Ma, Enhancement of Tensile Ductility and Stretch Formability of AZ31 Magnesium Alloy Sheet Processed by Cross-Wavy Bending, *J. Alloys Compd.*, 2013, **581**, p 230–235. <https://doi.org/10.1016/j.jallcom.2013.06.185>
50. X. Yang, Z. Sun, J. Xing, H. Miura, and T. Sakai, Grain Size and Texture Changes of Magnesium Alloy AZ31 During Multi-directional Forging, *Trans. Nonferrous Met. Soc. China*, 2008, **18**, p s200–s204. [https://doi.org/10.1016/S1003-6326\(10\)60202-6](https://doi.org/10.1016/S1003-6326(10)60202-6)
51. M. Janeček, M. Popov, M.G. Krieger, R.J. Hellmig, and Y. Estrin, Mechanical Properties and Microstructure of a Mg Alloy AZ31 Prepared by Equal-Channel Angular Pressing, *Mater. Sci. Eng. A*, 2007, **462**, p 116–120. <https://doi.org/10.1016/j.msea.2006.01.174>
52. S.M. Masoudpanah and R. Mahmudi, Effects of Rare-Earth Elements and Ca Additions on the Microstructure and Mechanical Properties of AZ31 Magnesium Alloy Processed by ECAP, *Mater. Sci. Eng. A*, 2009, **526**, p 22–30. <https://doi.org/10.1016/j.msea.2009.08.027>
53. M. Zimina, J. Bohlen, D. Letzig, G. Kurz, M. Cieslar, and J. Zník, The Study of Microstructure and Mechanical Properties of Twin-Roll Cast AZ31 Magnesium Alloy After Constrained Groove Pressing, *IOP Conf. Ser. Mater. Sci. Eng.*, 2014, **63**, p 012078. <https://doi.org/10.1088/1757-899X/63/1/012078>
54. Z. Wang, K. Wang, X. Wang, T. Wang, L. Zhu, and Y. Guan, Warm Tensile Deformation and Fracture Behavior of AZ31 Magnesium Alloy Sheets Processed by Constrained Groove Pressing, *J. Mater. Eng. Perform.*, 2020, **29**, p 7662–7677. <https://doi.org/10.1007/s11665-020-05220-y>
55. P.T. Thuy, D.T.H. Hue, D.M. Ngun, and P. Quang, A Study on Microstructure and Mechanical Properties of AZ31 Magnesium Alloy after Constrained Groove Pressing, *IOP Conf. Ser. Mater. Sci. Eng.*, 2019, **611**, p 012005. <https://doi.org/10.1088/1757-899X/611/1/012005>
56. P. Lin, T. Tang, Z. Zhao, W. Wang, and C. Chi, Refinement Strengthening of AZ31 Magnesium Alloy by Warm Constrained Groove Pressing, *Mater. Sci.*, 2017 <https://doi.org/10.5755/j01.ms.23.1.14392>
57. K. Soon Fong, M. Jen Tan, F. Lan Ng, A. Danno, and B. Wah Chua, Microstructure Stability of a Fine-Grained AZ31 Magnesium Alloy Processed by Constrained Groove Pressing During Isothermal Annealing, *J. Manuf. Sci. Eng.*, 2017 <https://doi.org/10.1115/1.4036529>
58. Q. Wang, Y. Mu, J. Lin, L. Zhang, and H.J. Roven, Strengthening and Toughening Mechanisms of an Ultrafine Grained Mg-Gd-Y-Zr Alloy Processed by Cyclic Extrusion and Compression, *Mater. Sci. Eng. A*, 2017, **699**, p 26–30. <https://doi.org/10.1016/j.msea.2017.05.080>
59. B. Sułkowski, M. Janoska, G. Boczkal, R. Chulist, M. Mroczkowski, and P. Pałka, The Effect of Severe Plastic Deformation on the Mg Properties After CEC Deformation, *J. Magnes. Alloy.*, 2020, **8**, p 761–768. <https://doi.org/10.1016/j.jma.2020.04.005>
60. P. Mansoor and S.M. Dasharath, Microstructural and Mechanical Properties of Magnesium Alloy Processed by Severe Plastic Deformation (SPD)-A Review, *Mater. Today Proc.*, 2020, **20**, p 145–154. <https://doi.org/10.1016/j.matpr.2019.10.088>

61. I.J. Beyerlein and L.S. Tóth, Texture Evolution in Equal-Channel Angular Extrusion, *Prog. Mater. Sci.*, 2009, **54**, p 427–510. <https://doi.org/10.1016/j.pmatsci.2009.01.001>
62. S. Yi, J. Bohlen, F. Heinemann, and D. Letzig, Mechanical Anisotropy and Deep Drawing Behaviour of AZ31 and ZE10 Magnesium Alloy Sheets, *Acta Mater.*, 2010, **58**, p 592–605. <https://doi.org/10.1016/j.actamat.2009.09.038>
63. A. Rollett, F. Humphreys, G.S. Rohrer, and M. Hatherly, *Recrystallization and Related Annealing Phenomena*, 2nd ed. Elsevier, 2004. <https://doi.org/10.1016/B978-0-08-044164-1.X5000-2>
64. T. Sakai, A. Belyakov, R. Kaibyshev, H. Miura, and J.J. Jonas, Progress in Materials Science Dynamic and Post-Dynamic Recrystallization Under Hot, Cold and Severe Plastic Deformation Conditions, *J. Prog. Mater. Sci.*, 2014, **60**, p 130–207. <https://doi.org/10.1016/j.pmatsci.2013.09.002>
65. M.R. Barnett, A Taylor Model Based Description of the Proof Stress of Magnesium AZ31 During Hot Working, *Metall. Mater. Trans. A*, 2003, **34**, p 1799–1806. <https://doi.org/10.1007/s11661-003-0146-5>
66. Q. Ma, B. Li, E.B. Marin, and S.J. Horstemeyer, Twinning-Induced Dynamic Recrystallization in a Magnesium Alloy Extruded at 450°C, *Scr. Mater.*, 2011, **65**, p 823–826. <https://doi.org/10.1016/j.scriptamat.2011.07.046>
67. É. Martin and J.J. Jonas, Evolution of Microstructure and Microtexture During the Hot Deformation of Mg–3% Al, *Acta Mater.*, 2010, **58**, p 4253–4266. <https://doi.org/10.1016/j.actamat.2010.04.017>
68. L. Jiang, J.J. Jonas, R.K. Mishra, A.A. Luo, A.K. Sachdev, and S. Godet, Twinning and Texture Development in Two Mg Alloys Subjected to Loading Along Three Different Strain Paths, *Acta Mater.*, 2007, **55**, p 3899–3910. <https://doi.org/10.1016/j.actamat.2007.03.006>
69. N.V. Dudamell, I. Ulacia, F. Gálvez, S. Yi, J. Bohlen, D. Letzig, I. Hurtado, and M.T. Pérez-Prado, Influence of Texture on the Recrystallization Mechanisms in an AZ31 Mg Sheet Alloy at Dynamic rates, *Mater. Sci. Eng. A*, 2011 <https://doi.org/10.1016/j.msea.2011.11.018>
70. A.S. Khan, A. Pandey, T. Gnäupel-Herold, and R.K. Mishra, Mechanical Response and Texture Evolution of AZ31 Alloy at Large Strains for Different Strain Rates and Temperatures, *Int. J. Plast.*, 2011, **27**, p 688–706. <https://doi.org/10.1016/j.ijplas.2010.08.009>
71. J. Koike, T. Kobayashi, T. Mukai, H. Watanabe, M. Suzuki, K. Maruyama, and K. Higashi, The Activity of Non-basal Slip Systems and Dynamic Recovery at Room Temperature in Fine-Grained AZ31B Magnesium Alloys, *Acta Mater.*, 2003, **51**, p 2055–2065. [https://doi.org/10.1016/S1359-6454\(03\)00005-3](https://doi.org/10.1016/S1359-6454(03)00005-3)
72. M.R. Barnett, M.D. Nave, and A. Ghaderi, Yield Point Elongation due to Twinning in a Magnesium Alloy, *Acta Mater.*, 2012, **60**, p 1433–1443. <https://doi.org/10.1016/j.actamat.2011.11.022>
73. W.F. Hosford and R.M. Caddell, *Metal Forming*, Cambridge University Press, 2007. <https://doi.org/10.1017/CBO9780511811111>
74. D.N. Lee, Relation Between Limiting Drawing Ratio and Plastic Strain Ratio, *J. Mater. Sci. Lett.*, 1984, **3**, p 677–680. <https://doi.org/10.1007/BF00719921>
75. X. Huang, K. Suzuki, A. Watazu, I. Shigematsu, and N. Saito, Improvement of Formability of Mg–Al–Zn alloy Sheet at Low Temperatures Using Differential Speed Rolling, *J. Alloys Compd.*, 2009, **470**, p 263–268. <https://doi.org/10.1016/j.jallcom.2008.02.029>
76. P.R. Tiwari, A. Rathore, and M.G. Bodkhe, Factors Affecting the Deep Drawing Process—A Review, *Mater. Today Proc.*, 2021 <https://doi.org/10.1016/j.matpr.2021.10.189>
77. Y.S. Lee, Y.N. Kwon, S.H. Kang, S.W. Kim, and J.H. Lee, Forming Limit of AZ31 Alloy Sheet and Strain Rate on Warm Sheet Metal Forming, *J. Mater. Process. Technol.*, 2008, **201**, p 431–435. <https://doi.org/10.1016/j.jmatprotec.2007.11.306>

Publisher's Note Springer Nature remains neutral with regard to jurisdictional claims in published maps and institutional affiliations.

Springer Nature or its licensor (e.g. a society or other partner) holds exclusive rights to this article under a publishing agreement with the author(s) or other rightsholder(s); author self-archiving of the accepted manuscript version of this article is solely governed by the terms of such publishing agreement and applicable law.